

Synthesis and characterization of iron oxide nanoparticles dispersed in mesoporous aluminum oxide or silicon oxide

Tiago Pinheiro Braga · Antônio Narcísio Pinheiro ·
W. T. Herrera · Y. T. Xing · E. Baggio-Saitovitch ·
Antoninho Valentini

Received: 22 November 2009 / Accepted: 29 July 2010 / Published online: 11 August 2010
© Springer Science+Business Media, LLC 2010

Abstract Iron oxide nanoparticles dispersed in aluminum (Al) or silicon (Si) oxides were prepared via a polymeric precursor derived from the Pechini method. The samples were characterized by thermogravimetric analysis, Fourier-transform infrared spectroscopy, X-ray diffraction, N₂ adsorption/desorption isotherms (Brunauer–Emmett–Teller, BET), Mössbauer spectroscopy, and vibrating sample magnetometry (VSM). BET analysis shows that the samples are mesoporous materials and have a high surface area. The size of the Fe₂O₃ nanoparticles in Al₂O₃ is smaller than that in SiO₂. Mössbauer spectra of the samples show that the Fe₂O₃ nanoparticles in Al₂O₃ are non-magnetic at room temperature but magnetic below 50 K. The FeSi samples are magnetic at both room and low temperatures. The magnetic measurements with VSM confirmed this point.

Introduction

It is well known that the properties of nanostructured materials differ strongly from those of bulk materials [1–4]. In particular, their properties are very much size-dependent and are critically sensitive to the methodologies employed to synthesize them [5, 6].

Nanostructured magnetic materials have attracted considerable interest both for fundamental research and for the technological applications [7]. Since a high number of atoms are located at surfaces or interfaces in nanoparticles, having reduced coordination and exhibiting high surface anisotropy, their magnetic properties are expected to be strongly modified when compared to the bulk materials [8]. Superparamagnetic effects are directly related to the exceptionally small size of magnetic nanoparticles, as reported in the literature [9].

Iron oxide is a convenient compound for the general study of the polymorphism and the mutual polymorphous changes in nanoparticles [10]. It also has many important applications in various industrial fields, such as gas sensors, catalysts, biomedicine, recording media, etc. [7, 11]. In the latter fields the use of small particles of iron oxides is of extreme importance. The advantage of using iron oxide nanoparticles relies on their chemical stability, in contrast to commonly used ultrafine particles of the pure metals [11].

There is a great interest at the moment in synthesis of iron oxides nanoparticles dispersed in silica matrix, which has potential application in information storage, magnetic refrigeration, magneto-optical solid devices, magnetic resonance imaging enhancement, and heterogeneous catalysts [12–14]. The magnetism and electrical properties of iron oxide in Al₂O₃–matrix also have been investigated recently due to its high potential application [15].

Most of these applications require well-dispersed and chemically stable nanoparticles. For this reason, new technologies in the synthesis and methods of analysis have been developed. Among the chemical methods which may be used for this objective, the polymeric precursor method derived from the Pechini method presents this characteristic [16, 17] and it shows very interesting results [18, 19].

T. P. Braga · A. N. Pinheiro · A. Valentini (✉)
Langmuir - Laboratório de Adsorção e Catálise, Departamento de Química Analítica e Físico-Química, Universidade Federal do Ceará, Campus do Pici, Fortaleza, CE CEP 60455-970, Brazil
e-mail: valent@ufc.br

W. T. Herrera · Y. T. Xing · E. Baggio-Saitovitch
Departamento de Física Experimental, Centro Brasileiro de Pesquisas em Física, Rua Dr. Xavier Sigaud 150, Rio de Janeiro, RJ CEP 22290-180, Brazil

In spite of the vast number of reports correlated to this or modified synthesis route [16–20], we report about the synthesis and characterization of nanoparticles of iron oxide embedded in aluminum (Al) or silicon (Si) oxides, prepared with the polymeric precursor method. The experimental results presented herein can provide information related to the studies of synthesis and characteristics of the iron oxide dispersed/embedded in Al or Si oxides, which are very important materials for the catalytic application.

Experimental procedure

Sample preparation

The samples were synthesized by the polymeric precursor method [16, 18]. This method is based on the chelation of cations (metals) by citric acid in a water solution. Al nitrate nonahydrate $\{\text{Al}(\text{NO}_3)_3 \cdot 9\text{H}_2\text{O}\}$, iron nitrate nonahydrate $\{\text{Fe}(\text{NO}_3)_3 \cdot 9\text{H}_2\text{O}\}$, tetraethylorthosilicate, citric acid monohydrate (CA) $\{\text{C}_6\text{H}_8\text{O}_7 \cdot \text{H}_2\text{O}\}$, and ethylene glycol (EG) $\{\text{C}_2\text{H}_6\text{O}_2\}$ were used as starting chemicals. A CA/metal ratio of 1.5:1 (mol) was used for all the samples. The metal amount is the sum of Fe, Al, and/or Si. The mass ratio of CA/EG was kept at 2:3. Samples with different Fe-to-Al and Fe-to-Si molar ratios were prepared and labeled FeAl-X and FeSi-X, where X denotes the Al:Fe and Si:Fe molar ratio.

For the synthesis process of the FeAl-14 sample, where 14 is the Al/Fe molar ratio, 0.070 and 0.005 mol of Al and Fe salts, respectively, were dissolved in distilled water at room temperature. CA (0.1125 mol) was dissolved in ethanol at 50 °C. Later the aqueous solution was added to the CA–ethanol solution and stirred during 15 min at 50 °C. Subsequently, the EG was added, and the mixture was stirred for 3 h at 100 °C until it became a viscous resin. The resin was treated at 200 °C for 1 h under air. The resulting precursor composite was milled and treated at 500 °C under air flow for 1 h.

Characterization

The pyrolysis step was followed by thermogravimetric analysis (TG), using a 10 °C/min heating rate, under an air flow of 50 mL/min and 10 mg of sample. The crystal structure of the metal oxides was characterized by X-ray diffraction (XRD) analysis, with Cu K α irradiation source ($\lambda = 1.5418 \text{ \AA}$, 30 kV, and 20 mA).

Specific surface area (Brunauer–Emmett–Teller, BET) and pore volume of the samples were determined by N₂ adsorption/desorption isotherms, at liquid nitrogen temperature. The samples (40–50 mg) were evacuated at

200 °C for 2 h prior to the experiments. The Fourier-transform infrared spectroscopy (FTIR) analyses were performed after the calcination process in the range from 400 to 4000 cm⁻¹ by using of KBr pellets containing 1.0 wt% of the sample.

Transmission Mössbauer spectra were recorded at room temperature in constant acceleration mode setup, with a ⁵⁷Co (Rh) source. The Mössbauer data were fitted to discrete Lorentzian functions, using the least-square fitting routine of the NORMOS® software package. All isomer shift (IS) values (δ) are quoted relatively to αFe .

The magnetic properties of the samples were studied using a new Cryofree Quantum Design equipment (vibrating sample magnetometry, VSM), based on the fluxmeter method connected to a data acquisition computing system (PC), at wide range of temperature (5–300 K) and at fields ranging from 0 to 15 kOe.

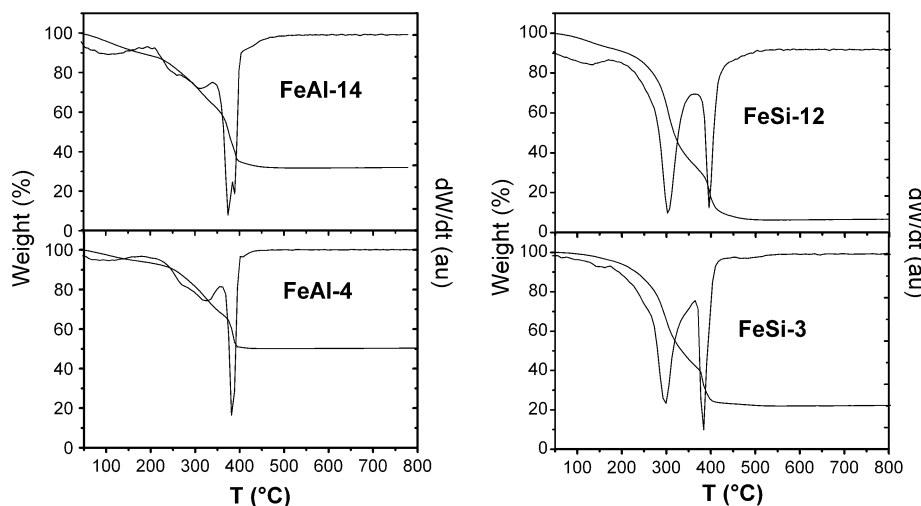
Results and discussion

The thermal analysis result, presented in Fig. 1, indicates three main events. The weight elimination in the range 40–200 °C, with a maximum of around 100 °C, is related to the volatile compounds (water) adsorbed in the surface of the samples. In the second temperature range (between 200 and 500 °C), the decomposition of the residual organic material is favored [16, 18] and shows two peaks in the DTG profile. The event observed near 290 °C is probably due to the partial organic precursor decomposition during the sample preparation (heat treated at 200 °C). Such temperature of heat treating may result in a sample which presents high amounts of oxygen in the composition of the residual material. On the other hand, the peak in the DTG profile observed near 400 °C is probably related to the residual organic substance decomposition, but with low amount of oxygen in the composition [21].

It is interesting to point out, in Fig. 1, the percentage of residual weight loss for the samples. The increase of iron ratio in the sample composition promotes a lowering in the residual weight elimination. A similar behavior is observed due to the change of the support precursor (Al or Si). The iron likely works as a catalyst in the precursor elimination during the heat treatment at 200 °C.

Such a statement suggests that the difference of the metal ratio (Fe), as well as the nature of the component used as support (Al or Si), can affect the final morphology of the samples after the thermal treatment (surface area, diameter, and volume of pores), as indicated in previous study [21, 22]. The morphological behavior displayed by the material is mainly due to the use of organic compounds (CA and EG) in the preparation of the materials, since in the removal of volatile materials, eliminated during the

Fig. 1 TG profile and the respective DTG of the precursors of the materials



pyrolysis step, results in cavities and simultaneous rearrangement of the solid.

By applying nitrogen adsorption/desorption isotherms, which are presented in Fig. 2, the diameter (D_p) and volume (V_p) of pore were determined, as well as the surface area (S) of the synthesized materials. The isotherm profiles point to a heterogeneous porosity (a mixture of type IV and type II, according to IUPAC classification). On the other hand, while the samples FeAl-14 and FeSi-12 show a predominance of type IV with H₂ hysteresis loop, in the samples FeAl-4 and FeSi-3 there is a high proportion of isotherms type II, characteristic of mesoporous powders (H₃ hysteresis loop), which are interesting for some processes (catalysis and adsorption).

The profiles of pore diameter distribution presented in Fig. 2b (according to the BJH method) exhibit a broad pore size distribution, with the majority of the porous diameter located in the range from 30 to 150 Å.

An increase in the amount of iron in the sample composition promoted changes in the hysteresis behavior, which can be attributed to the closing of the pores by iron oxide. Table 1 lists the values of the surface area, total pore volume, and the average pore diameter of the samples, which points to the textural effect, promoted by an increase in the amount of iron.

Such textural effects in the porosity of the synthesized solids may be related to the information evidenced in the TG analysis (Fig. 1). Samples with higher iron amount were seen to demonstrate a lower ratio of residual organic substances. After the calcination process, according to the isotherm curves, this can result in differences in the characteristics of the pores [21], which are perceptible in the values of the surface area, volume, and diameter of pore.

The FTIR spectra of the materials after the calcinations process at 500 °C are presented in Fig. 3. These profiles

points to the presence of carbonate and water. The carbonate vibrations bands of C–O (1420 cm⁻¹), however, are probably due to the carbon dioxide adsorbed in the solid surface since the Fe, Si, and Al carbonates decomposed at approximately 350 °C [23]. Two bands appear at 3600 and 1640 cm⁻¹ due to O–H vibrations of water. The presence of H₂O and CO₂ is probably due to the exposure of samples to atmospheric air after the calcination process at 500 °C. Furthermore, a band associated with the M–O–H group stretching is observed at approximately 1100 cm⁻¹, and the M–O and M–O–M bond vibrations are observed in the range 800–450 cm⁻¹ [11, 23, 24].

The spectroscopy results reveal some differences to the change of the support precursor (Al or Si). The broad band for the samples supported in Al at 580 cm⁻¹ is attributed to the Fe–O vibration. On the other hand, the band at 460 cm⁻¹ can be associated with M–O bonds (M = Fe or Si) for the samples containing Si. Additionally, the band at 800 cm⁻¹ for the samples FeSi-12 and FeSi-3 is probably associated with the O–Si–O bond and the band around 960 cm⁻¹ for the sample FeSi-3 is due to the Si–OH groups [14, 24].

FTIR spectroscopy is an apparatus very important to characterize the stretching vibrations to the metal oxides, but not sufficient for identification of crystalline phases. In order to achieve more information about the crystal structure of the samples, XRD analysis was carried out.

After the calcination process carried out at 500 °C under air flow, as suggested by the TG analysis, the samples were submitted to the XRD. The results are presented in Fig. 4.

The FeAl-14 sample presented the profile of an amorphous solid, whereas the FeAl-4 sample showed broader peaks, a fact that which can be assigned to a small crystal. The 2θ degree value of the broader peaks and the relative intensities suggest the Al₂O₃ phase formation for the FeAl-4 sample. Such low coherence lengths obtained from

Fig. 2 N₂ adsorption/desorption isotherms (a), and pore diameter distribution (b)

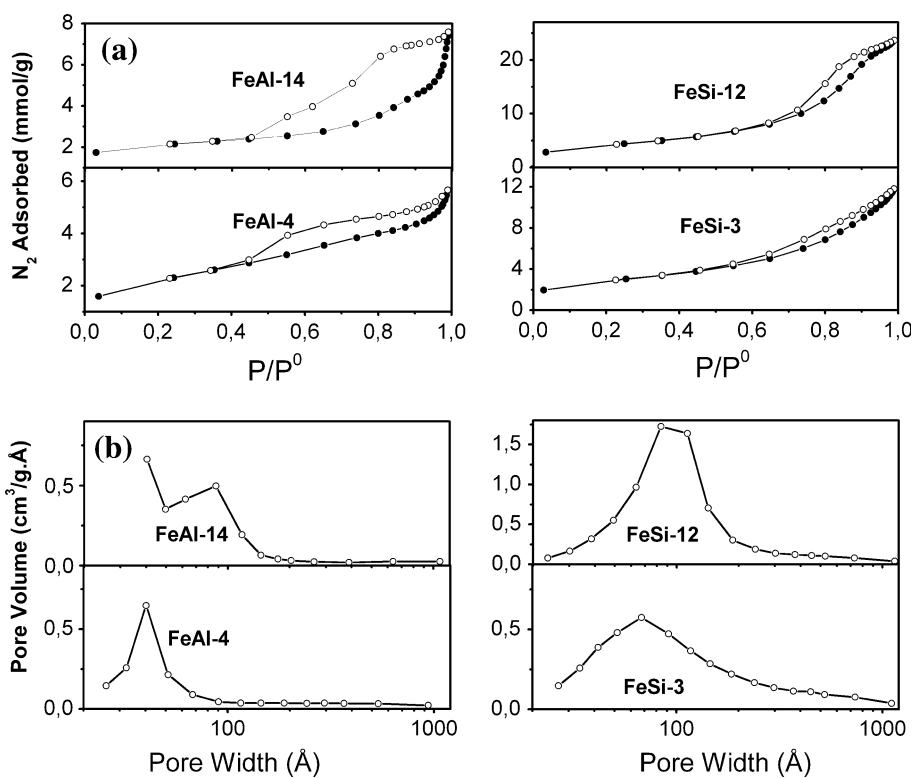


Table 1 Textural properties of the samples determined by N₂ adsorption isotherms

Samples	<i>S</i> (m ² /g)	<i>V</i> _p (cm ³ /g)	<i>D</i> _p (Å)
FeAl-14	145	0.23	65
FeAl-4	166	0.18	49
FeSi-12	323	0.80	83
FeSi-3	217	0.39	75

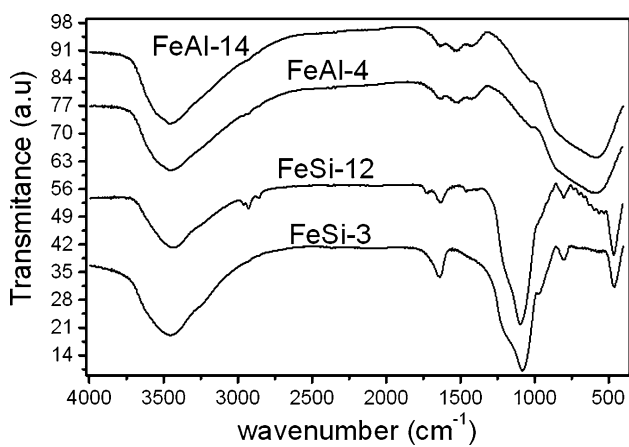


Fig. 3 Profile of FTIR spectroscopy of the samples after calcination

X-ray line broadening may arise due to multiple contributions from particle size and shape defects including mesopores, dislocations, and point defects.

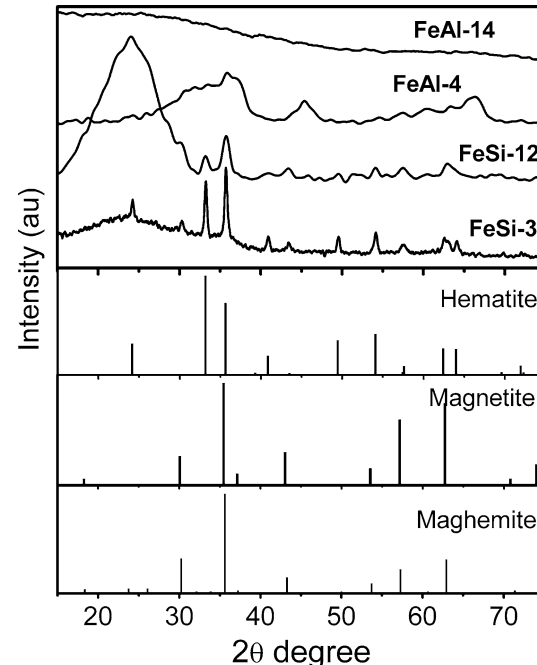


Fig. 4 XRD profile of the samples after calcination process under air flow

On the other hand, the FeSi-12 and FeSi-3 samples showed the pattern of hematite (α -Fe₂O₃, JCPDS 86-2368). In addition, the FeSi-3 sample profile suggests the presence of maghemite phase (γ -Fe₂O₃, JCPDS 39-1346).

This apparent Al influence in the hematite crystallization can be assigned to the ionic radii. The radii of Al^{3+} (0.57 Å) species is closer to the radii of Fe^{3+} (0.67 Å) species, if compared to Si^{4+} (0.39 Å). The similar ionic radii enable the insertion of Al^{3+} into the lattice in place of Fe^{3+} , which makes the hematite crystallization difficult. Nevertheless, if the hematite phase is formed in the FeAl-14 and FeAl-4 samples, its crystal size is very small [25].

In spite of the low crystalline organization presented by the samples, the Rietveld method [26] was applied for the refinement of the diffraction profile of the samples FeSi-12 and FeSi-3. DBWS9807 program described by Young et al. [27] was applied. By this method, it was possible to relatively quantify the different phase formed, and the results are displayed in Table 2. The crystallite sizes of the samples were calculated from the XRD data using the Debye-Scherrer for all the reflections of the XRD profiles. The calculated results indicate that the resultants are the nanometer-sized crystalline powders and the average grain sizes are listed in Table 2.

It is known that in case of iron oxide there is a little difference in the lattice parameters of the two phases and due to the small size of the particles they are poorly resolved. In such cases XRD is necessary but not sufficient tool for the characterization of powders of iron oxide. Therefore, additional technical such as Mossbauer spectroscopy are indispensable.

The local environment of iron atoms in the iron-containing samples was investigated by Mössbauer spectroscopy (MS) (Fig. 5). The room temperature spectra obtained for samples FeAl-4 and FeSi-3 (Fig. 5) show similar central doublet with small IS, relative to $\alpha\text{-Fe}$, around 0.30 and 0.32 mm/s, respectively. The quadrupole splittings of 1.00 and 0.94 mm/s, respectively, are typical of Fe^{3+} ions dispersed in silica or Al_2O_3 matrix. The absence of magnetic sextets in the FeAl-4 sample suggests that all iron oxide nanoparticles are in a superparamagnetic regime, and in the FeSi3 sample only 60% of them are in the regime. Therefore, the Mössbauer spectra obtained at 4.2 K corroborates the assumption that Fe-based phases are not identifiable by XRD for samples containing Al due to the extremely small particle sizes.

Table 2 Relative weight percentage of phases and grain size

Samples	Crystalline phase (wt%)			Grain size (nm)		
	Al_2O_3	$\alpha\text{-Fe}_2\text{O}_3$	$\gamma\text{-Fe}_2\text{O}_3$	Al_2O_3	$\alpha\text{-Fe}_2\text{O}_3$	$\gamma\text{-Fe}_2\text{O}_3$
FeAl-14	—	—	—	—	—	—
FeAl-4	—	—	—	—	—	—
FeSi-12	—	100.0	—	—	3.5	—
FeSi-3	—	11.5	88.5	—	4.1	13.2

For the sample FeSi-3, on the other hand, it was observed two sextets very close to one another. One six-line subspectrum with IS, relative to $\alpha\text{-Fe}$, $\delta = 0.34$ mm/s, quadrupole shift $\varepsilon = -0.20$ mm/s, and magnetic hyperfine field $B_{hf} = 51.5$ T it is typical of hematite [28, 29] and the other one with $\delta = 0.34$ mm/s, quadrupole shift $\varepsilon = -0.1$ mm/s, and $B_{hf} = 50$ T typical of maghemita [30]. Hence, the observed Mössbauer spectrum is a contribution from $\alpha\text{-Fe}_2\text{O}_3$ and $\gamma\text{-Fe}_2\text{O}_3$.

Therefore, in addition with XRD analysis (Fig. 4), it confirms the existence of very fine-grained $\alpha\text{-Fe}_2\text{O}_3$ and $\gamma\text{-Fe}_2\text{O}_3$ phase in the sample FeSi-3, whereas the doublets observed in the Mössbauer spectra suggesting that the iron phases are in a superparamagnetic state. These observations are consistent with results recently published [30–32].

MS represents a fundamental tool in order to investigate the magnetic behavior of nanoparticles and additional information can be obtained with measurements for different temperatures. However, supplementary technical such as vibrating sample magnetometer is essential to help the results obtained by MS.

The results of the magnetization measurement are presented in Fig. 6. The room temperature curve for sample FeAl-4 shows that the sample is paramagnetic and it is not saturated with the applied external magnetic field, which is in agreement with the MS results as shown in Fig. 5. Since the sample contains fine (3.5 at 14.2 nm) nanoparticles, the result suggests that the nanoparticles are in superparamagnetic state. The low temperature measurement confirmed the conclusion. At 50 K, the M-H curve of the FeAl-4 sample is till almost a strait line but the center of the curve opened as shown in the inset (a) of Fig. 6, which is a typical behavior of a strong antiferromagnetic material. The results here show that when the temperature decreased from room temperature to 50 K, the sample has a transition from superparamagnetic state to a strong antiferromagnetic state. This is also in agreement with the MS results in Fig. 5. As it well known that the $\alpha\text{-Fe}_2\text{O}_3$ has a first-order phase transition from canted antiferromagnetic to fully antiferromagnetic state, which is usually called Morin transition. The Morin transition takes place at the temperature ~ 263 K in bulk materials. Crystal defects, strains, stoichiometric deviations, and surface effects also tend to reduce the Morin temperature (T_M) and it decreases with decreasing the particle size [33–35]. Our study of pure Fe_2O_3 nanoparticles shows that the Morin transition temperature of 50 nm particles is around 220–250 K (unpublished). For the Fe_2O_3 nanoparticles in this article, from the MS and VSM results one can know that they are strong antiferromagnetic below 50 K. In this case we can conclude that T_M of the FeAl sample is higher than 50 K but below 300 K.

The profile of Mossbauer spectra (Fig. 5a) point to near 50% of the spectra is blocked while the other part is in

Fig. 5 ^{57}Fe Mössbauer spectra for the samples at different temperature (300 and 4.2 K)

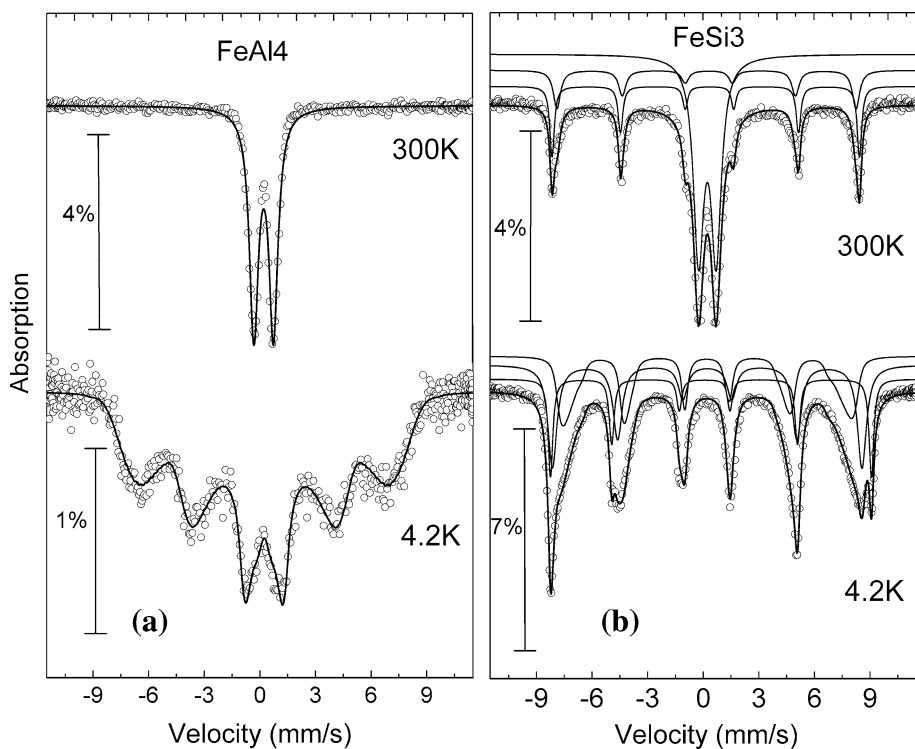
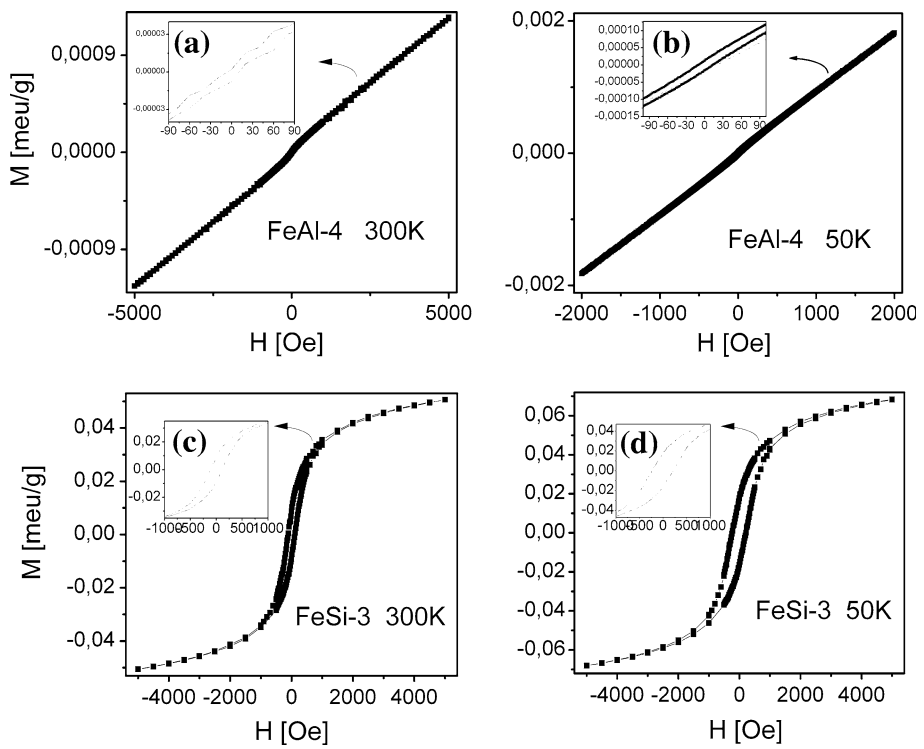


Fig. 6 Magnetization measurement at different temperature (300 and 50 K). Inset: (a–d) expanded magnetization curves showing hysteresis for the samples



release process, which suggests that the blocking temperature (T_b) of the superparamagnetism in this sample is 4.2 K. It is not possible to determine directly the Morin temperature (T_M) with the magnetization measure, because

the character superparamagnetic of FeAl-4 sample domain e blinded this information (Figs. 6a and 7).

On the other hand, the sample FeSi-3 is very different: it points to a little hysteresis at room temperature; therefore,

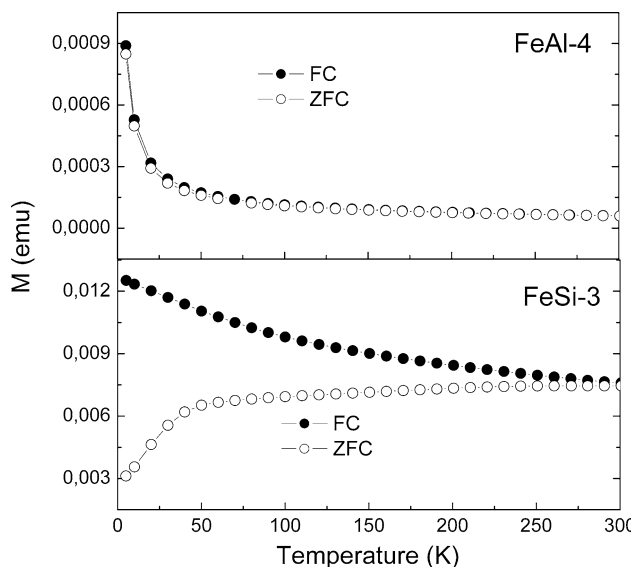


Fig. 7 Temperature dependence of the ZFC (open symbols) and field-cooled (solid symbols) magnetization measured in a field of 100 Oe

the sample FeSi-3 does not show an ideal superparamagnetic behavior. The hysteresis can be from some big $\alpha\text{-Fe}_2\text{O}_3$ and $\gamma\text{-Fe}_2\text{O}_3$ particles, which is ferromagnetic at room temperature. The result agrees with the exposed in Fig. 2, which shows that the size distribution in FeSi-3 is much broader than that of FeAl-4 sample and the particles size is much bigger too. It also agrees with the Mössbauer spectra, as shown in Fig. 5, which presented a superparamagnetic doublets and one six-line subspectrum. Both of the Mössbauer spectra and the magnetic measurements show that the microstructure of the Fe_2O_3 nanoparticles is different from the particles in FeAl-4. The hysteresis and saturating behavior is usually from $\gamma\text{-Fe}_2\text{O}_3$ and the superparamagnetic signal in the Mössbauer spectra can be from the smaller particles of both $\alpha\text{-Fe}_2\text{O}_3$ and $\gamma\text{-Fe}_2\text{O}_3$. The M-H curves indicate that big part of the Fe_2O_3 nanoparticles in FeSi-3 are $\gamma\text{-Fe}_2\text{O}_3$ but in FeAl-4 all the particles are $\alpha\text{-Fe}_2\text{O}_3$, which is in good agreement with the XRD results as shown in Table 2. The M value of FeAl-4 is one order of magnitude smaller than the M value of FeSi-3 with very similar Fe ratio in the two samples. The difference is also easy to understand: it is attributed to the canted and fully antiferromagnetic ordering of the $\alpha\text{-Fe}_2\text{O}_3$ in FeAl-4.

On the other hand, in the Fig. 7 (sample FeSi-3), it is observed a little change in the ZFC profile near to 250 K, it may point to the T_M for the blocked particle group of the FeSi sample, as pointed by the MS. The same was not possible to be determined for the FeAl sample, for having superparamagnetic particle around this temperature.

The measured values for the sample FeSi-3 at 300 K are $H_C = 110.01$ Oe, $M_r = 0.84$ emu/g, and $M_s = 4.94$ emu/g. The above results exhibit remarkable discrepancies in the

magnetic properties; therefore, the difference of the metal ratio (Fe), as well as the nature of the component used as support (Al or Si), can affect the magnetic properties.

The XRD, MS, and magnetization measurement are in a quite good agreement. The corroboration of these data allows the following description of the prepared samples containing nanoparticles and a superparamagnetic phenomenon.

Conclusion

The synthesis method used enables the preparation of materials containing nanoparticles mesoporous of iron oxide, which present a superparamagnetic phenomenon dispersed in a mesoporous matrix. Depending on the matrices (Al or Si) we can get completely $\alpha\text{-Fe}_2\text{O}_3$ nanoparticles or a mixture of $\alpha\text{-Fe}_2\text{O}_3$ and $\gamma\text{-Fe}_2\text{O}_3$. Therefore, the characteristic observed for the materials synthesized suggests its application in catalysis, gas sensors, technological processes, and in the biomedical areas.

Acknowledgements The authors acknowledge the “Universidade Federal do Ceará” (UFC), CNPq/CT-PETRO, Dr. J. M. Sasaki (Laboratório de Raios X) for the DRX measurements. T. P. Braga and A. N. Pinheiro express gratitude for the scholarship from CAPES and CNPq. E Saitovitch acknowledges support from CNPq and FAPERJ (Cientista do Estado, PRONEX-FAPERJ and Pensa-Rio) for grants.

References

1. Coey JMD (1971) Phys Rev Lett 25:1140
2. Morup S, Tronc E (1994) Phys Rev Lett 72:3278
3. Martinez B, Obradors X, Balcells L, Rovonet A, Monty C (1998) Phys Rev Lett 80:181
4. Bødker F, Hansen MF, Bender Koch C, Lefmann K, Morup S (2000) Phys Rev B 61:6826
5. Nagar H, Kulkarni NV, Karmakar S, Sahoo B, Banerjee I, Chaudhari PS, Pasricha R, Das AK, Bhoraskar SV, Date SK, Keune W (2008) Mater Charact 59:1215
6. Shafi KVPM, Ulman A, Dyal A, Yan X, Yang NL, Estournes C (2002) Chem Mater 14:1778
7. Hong RY, Fu HP, Di GQ, Zheng Y, Wei DG (2008) Mater Chem Phys 108:132
8. Weller H (1993) Adv Mater 5:88
9. Chen Q (1999) J Magn Magn Mater 194:1
10. Zboril R, Mashlan M, Petridis D (2002) Chem Mater 14:969
11. Gang Z, Kaihua S, Defeng Z, Yukun Y, Guangyu W (2008) Mater Lett 62:219
12. Teja AS, Koh P-Y (2009) Prog Cryst Growth Charact Mater 55:22
13. Corr SA, Gun'ko YK, Douvalis AP, Venkatesan M, Gunning RD, Nellist PD (2008) J Phys Chem C 112:1008
14. Cecilia S, Mihaela P, Corina E, Hrianca I (2002) Solid State Ionics 151:219
15. Mei L, Haibo L, Li X, Wenxue Y, Yang L, Zhudi Z (2005) J Magn Magn Mater 294:294
16. Valentini A, Carreño NLV, Leite ER, Longo E (2006) Appl Catal A 310:174

17. Montemayor SM, García-Cerda LA, Torres-Lubián JR, Rodríguez-Fernández OS (2008) Mater Res Bull 43:1112
18. Dominko R, Conte DE, Hanzel D, Gaberscek M, Jamnik J (2008) J Power Sources 178:842
19. Valentini A, Carreño NLV, Leite ER, Longo E (2003) Appl Catal A 255:211
20. Hao YW, Wang J, Chen ZY (2010) J Mater Sci 45:1361. doi: [10.1007/s10853-009-4092-5](https://doi.org/10.1007/s10853-009-4092-5)
21. Valentini A, Carreño NLV, Leite ER, Longo E (2004) Micropor Mesopor Mater 68:151
22. Braga TP, Elis CCG, Adriano FS, Neftali LVC, Valentini A (2009) J Non-Cryst Solids 355:860
23. Barrado E, Rodríguez JA, Prieto F, Medina J (2005) J Non-Cryst Solids 351:906
24. Braga TP, Longhinotti E, Pinheiro AN, Valentini A (2009) Appl Catal A 362:139
25. Jarvinen M (1993) J Appl Crystallogr 26:525
26. Rietveld HM (1967) J Appl Crystallogr 2:65
27. Young RA, Sakthivel A, Moss TS, Paiva-Santos CO (1995) J Appl Crystallogr 28:366
28. Annersten H, Hafner SS (1973) Crystallography 137:321
29. Predoi D, Crisan O, Jitianu A (2007) Thin Solid Films 515:6319
30. An SY, Shim I, Kim CS (2005) J Appl Phys 97:10Q909
31. Alexandre SA, José DF, Joseph WS (2008) Appl Clay Sci 39:172
32. Malina R, Silvia MH (2008) J Non-Cryst Solids 354:624
33. Sreeja V, Joy PA (2007) Mater Res Bull 42:1570
34. Vollath D, Szab DV, Taylor RD, Willis JO, Sickafus ILE (1995) Nanostruct Mater 6:491
35. Radhakrishnan S, Saujanya C, Sonar P, Gopalkrishnan IK, Yakhmi JV (2001) Polyhedron 20:1489